Oxygen Reduction Hot Paper

How to cite: Angew. Chem. Int. Ed. 2020, 59, 14639–14646
International Edition: doi.org/10.1002/anie.202006175
German Edition: doi.org/10.1002/ange.202006175

Cross-Linked Polyphosphazene Hollow Nanosphere-Derived N/P-Doped Porous Carbon with Single Nonprecious Metal Atoms for the Oxygen Reduction Reaction

Xuan Wei, Diao Zheng, Ming Zhao, Hongzhong Chen, Xun Fan, Bin Gao, Long Gu, Yi Guo, Jianbin Qin, Jing Wei, Yanli Zhao,* and Guangcheng Zhang**

Abstract: *Heteroatom-doped polymers or carbon nanospheres have attracted broad research interest. However, rational synthesis of these nanospheres with controllable properties is still a great challenge. Herein, we develop a template-free approach to construct cross-linked polyphosphazene nanospheres with tunable hollow structures. As comonomers, hexachlorocyclotriphosphazene provides N and P atoms, tannic acid can coordinate with metal ions, and the replaceable third comonomer can endow the materials with various properties. After carbonization, N/P-doped mesoporous carbon nanospheres were obtained with small particle size (≈50 nm) and high surface area (411.60 $m^2 g^{-1}$). Structural characterization confirmed uniform dispersion of the single atom transition metal sites (i.e., Co-N_2P_2) with N and P dual coordination. Electrochemical measurements and theoretical simulations revealed the oxygen reduction reaction performance. This work provides a solution for fabricating diverse heteroatom-containing polymer nanospheres and their derived single metal atom doped carbon catalysts.*

Introduction

Cross-linked polyphosphazenes with stable reticular covalent frameworks and rich heteroatoms have attracted broad attention in the past decade.[1] Here, hexachlorocyclotriphosphazene (HCCP) rings are conjugated by nucleophilic substitution of versatile aromatic organic monomers with dual/multi-nucleophilic groups through facile one-step precipitation polycondensation to fabricate cross-linked matrices.[2] Using different monomers, for instance, 4,4′-(hexafluoroisopropylidene)diphenol, melamine, and fluorescein (FL), the products would be endowed with different properties such as super-hydrophobicity, flame retardance, and fluorescence.[3] In addition, products with different morphologies including nanotubes, nanofibers, and microspheres can be obtained by tuning the reaction conditions.[4] To date, most of the cross-linked polyphosphazene microspheres were synthesized using other inorganic/organic spheres as sacrificial templates, resulting in hollow structures.[5] Due to the complex preparation and post-treatment process of the above microspheres and their size limitation caused by the templates, it is still a huge challenge to simply prepare nano-sized hollow polyphosphazene spheres without using a template.

As one of most abundant plant polyphenols, tannic acid (TA) is an easily accessible renewable resource.[6] Because of its biocompatibility, oxidation resistance, antibacterial and anti-inflammation properties, and strong affinity with biomacromolecules such as DNA, collagen, gelatin and thrombin, TA has been employed to prepare numerous biomaterials.[7] The high affinity between TA and biomacromolecules is attributed to multiple hydrogen bonds formed between the phenolic hydroxyl-rich moieties and target objects.[8] Additionally, with five galloyl groups and five catechol groups on each molecule, TA can coordinate with different kinds of metal ions to form metal–organic coordination polymers (MOCs).[9] These MOCs have recently been used as sacrificial templates to fabricate porous metal–carbon frameworks.[10] Because of the low cost and non-toxicity properties of TA, the derived carbon composites can be employed as efficient nonprecious metal catalysts for the oxygen reduction reaction (ORR), which is of great significance for the development of commercially viable fuel cell technologies.[11] However, the size of the metal nanoparticles in the metal-polyphenol complex derived carbon composites is uncontrollable. This is mainly because that the polyphenol derived carbon materials do not contain heteroatoms such as nitrogen and phosphorus to effectively stabilize metal atoms during the pyrolysis process. Therefore, it is important to prepare heteroatom-doped metal-TA coordination materials with controllable morphologies and stable chemical structures.

Herein, we present novel covalently cross-linked poly(HCCP-TA-BPS) (BPS = 4,4′-sulfonyldiphenol) nano-

[*] X. Wei, M. Zhao, X. Fan, Dr. J. Qin, Prof. G. Zhang
Shaanxi Key Laboratory of Macromolecular Science and Technology, School of Chemistry and Chemical Engineering, Northwestern Polytechnical University
Xi'an, Shaanxi 710072 (P. R. China)
E-mail: zhangguc@nwpu.edu.cn

D. Zheng
Analytical & Testing Center of Northwestern Polytechnical University
Xi'an, Shaanxi 710072 (P. R. China)

X. Wei, Dr. H. Chen, B. Gao, Dr. L. Gu, Dr. Y. Guo, Prof. Y. L. Zhao
Division of Chemistry and Biological Chemistry, School of Physical and Mathematical Sciences, Nanyang Technological University
21 Nanyang Link, 637371 Singapore (Singapore)
E-mail: zhaoyanli@ntu.edu.sg

Prof. J. Wei
The Key Laboratory of Biomedical Information Engineering of Ministry of Education, School of Life Science and Technology, Xi'an Jiaotong University
Xi'an, Shaanxi 710049 (P. R. China)
E-mail: jingwei@xjtu.edu.cn

Supporting information and the ORCID identification number(s) for the author(s) of this article can be found under: https://doi.org/10.1002/anie.202006175.

spheres (PSTA) with tunable hollow structures prepared through a one-step synthesis under ambient temperature. TA as a co-monomer to prepare cross-linked polyphosphazene materials has not been reported before. The polycondensation of HCCP with TA is more complicated than that with other monomers having few (2–4) nucleophilic groups. The key feature of this approach is to control the polymerization rate of TA and HCCP by reducing the activity of TA to obtain the products in a highly uniform morphology. Different from previously reported polyphosphazene spheres and hollow spheres, the size of PSTA is around 50 nm, which is much smaller. In addition, hollow spherical structures can be obtained by simply adjusting the reaction conditions, without using any external template. Because of the large steric hindrance of the TA molecule, it is difficult to achieve that the cross-linking reaction between TA and HCCP completely consumes the active groups. A third co-monomer with dual/multi-nucleophilic groups should be used for the substitution of unreacted Cl groups in HCCP to endow the spheres with new properties. Furthermore, the unreacted catechol groups on TA can chelate with metal ions. At last, N/P co-doped mesoporous carbon nanospheres with single metal atoms and high specific surface area (411.60 $m^2 g^{-1}$) were obtained through carbonization at 1000 °C. The catalysts exhibited high electrocatalytic activity and stability for ORR due to unique hollow porous structure and well-dispersed single metal sites.

Results and Discussion

The route for the synthesis of PSTA nanospheres is depicted in Figure 1a. Triethylamine (TEA) as an acid-binding agent was added excessively into a flask containing TA in acetonitrile. During the ultrasonic process, TA reacted with TEA to form primary nanosphere cores (polyTA). The activated hydroxyl groups on TA were then interacted with HCCP bearing chlorine groups. The polycondensation generated TA-HCCP oligomers and HCl byproduct that can be removed by the excessive amount of TEA to accelerate the polycondensation rate. Because of the high interface energy of the primary nanosphere cores, the TA-HCCP oligomers were easily seized on their surface and accumulated to form shells. Consequently, the cross-linked PSTA nanospheres were produced under the process of polymerization.

The monomer concentration, reaction temperature, and ultrasonic power effect on the formation of the PSTA nanomaterials were investigated in detail (Figure S1–S3 in the Supporting Information). Figure 1b shows the morphology of PSTA nanospheres synthesized under 160 W ultrasonication and circumstance temperature of 35 °C using different concentrations of monomers. With the increase of TA concentration from 0.5 $g L^{-1}$ to 5 $g L^{-1}$, the products transformed from solid nanospheres (SPSTA) to hollow nanospheres, and the hollow portion gradually grew larger. With the further increase of the TA concentration, products with bowl like morphology were obtained. This result is caused by the rupture of the spherical shell.

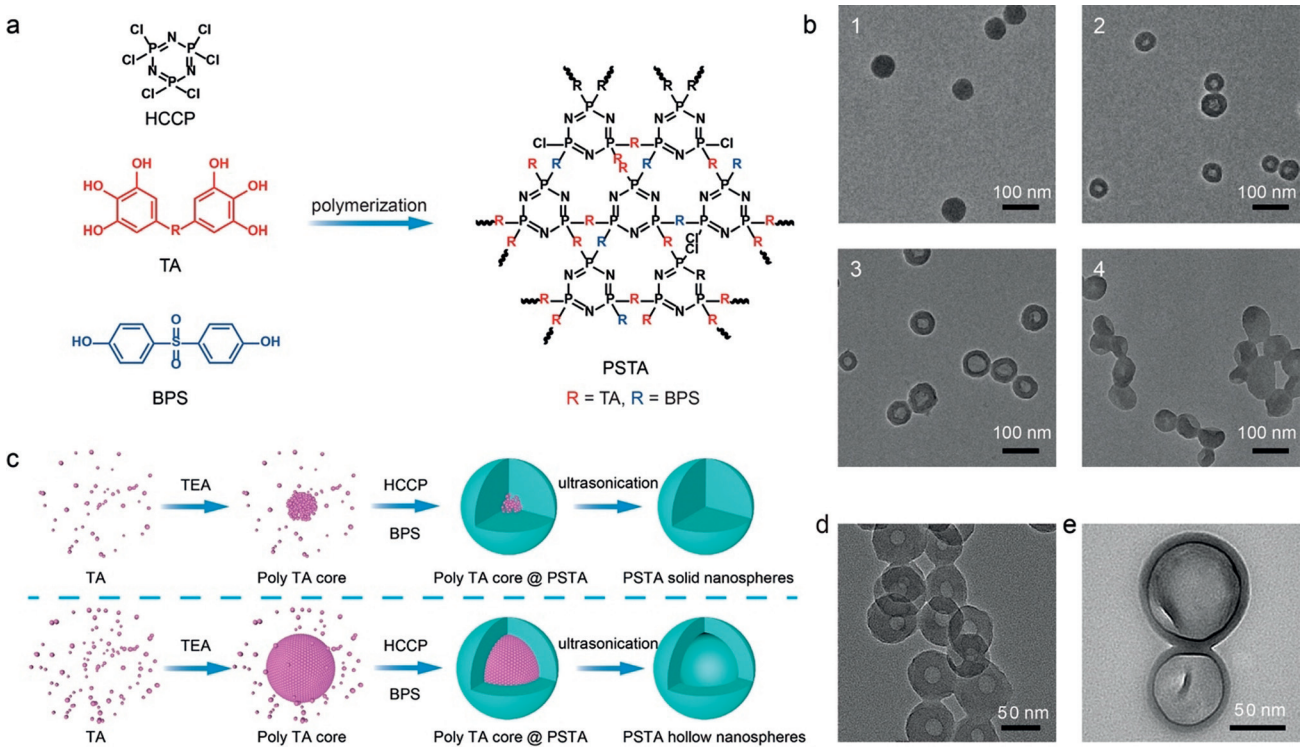

Figure 1. a) Synthesis of PSTA. b) TEM images of PSTA. c) Formation mechanism of PSTA solid nanosphere and hollow nanosphere. TEM images of d) poly(FL-co-TA-co-HCCP) and e) poly(HPS-co-TA-co-HCCP) hollow nanospheres.

The formation mechanism of the PSTA hollow nanospheres was further investigated by means of transmission electron microscopy (TEM). The products at variable stages of polymerization were examined (Figure S4). After TEA was added into the TA solution and sonicated for 30 min, spherical nanoparticles with diameters of 10–50 nm were observed, indicating the formation of polyTA core by the interaction of TA and TEA. HCCP and BPS were then added to the polycondensation with free TA in solution, and the formed polyTA cores have a large amount of active phenolic hydroxyl groups on their surface. The HCCP-TA-BPS oligomers adsorbed on the surface of polyTA cores eventually formed covalently cross-linked nanoshell. The polyTA cores were not stable enough to withstand the ultrasonication in ethanol and water after the polymerization, and thus the hollow structure was obtained. According to this mechanism, the primary polyTA cores would grow to form individual nanospheres. The size of the hollow cavity is determined by the size of the unstable primary polyTA cores. When the temperature and the power of the ultrasonication are constant, the amount of the initial unstable cores is invariable whatever the concentration of the monomer is. Relatively, higher TA concentration would produce more oligomers, which would then adsorb on the unstable cores and lead to larger hollow structures in the end (Figure 1 c). When the ultrasonication power or the temperature increases, solid nanospheres are obtained. This is because that the reactivity of HCCP and TA increases under high temperature or high power condition. TA and TEA in polyTA cores also participate in the polycondensation as the comonomer and acid acceptor, respectively, thereby causing the structure of the cores collapsed and replaced by the cross-linked polyphosphazene to form solid nanospheres. On the other hand, hollow nanospheres with thinner shells were obtained at lower temperature or ultrasonic power. Because of the low probability of oligomer collision in a low energy environment, products with non-uniform particle size distribution were fabricated.

As a comonomer in PSTA nanospheres, the main function of BPS is to substitute the unreacted Cl group in HCCP and make the cross-linked chemical structure more stable. BPS can be replaced by other aromatic organic monomers with dual/multi-nucleophilic groups to form new cross-linked polyphosphazene nanomaterials with a variety of special properties such as fluorescence, reactive oxygen species generation, and superhydrophobicity. These monomers can copolymerize with TA and HCCP in the ternary synthetic strategy.

As an illustration, FL was used as a comonomer to synthesize poly(FL-co-TA-co-HCCP) hollow nanosphere. In contrast, poly(FL-co-HCCP) hollow microsphere without TA component was synthesized as a control group under the conventional method. TEM characterizations showed that they were hollow spheres with particle sizes of 50 nm and 500 nm, respectively (Figure 1 d and S5). Fluorescence emission spectra (excited at 365 nm) exhibited that the two products had similar fluorescence properties (Figure S6). A more interesting phenomenon was observed when using bis-(4-hydroxyphenyl)-disulfide (HPS) as a comonomer to replace BPS. So far, the preparation of poly(HPS-co-HCCP) hollow spheres has not been reported in the literature, because the disulfide bond is unstable and can be easily destroyed during the formation of hollow structures. When using the template method, the etching process is very rapid and would cause severe damage to the structure, as shown in Figure S7. However, through the method discovered herein, poly(HPS-co-TA-co-HCCP) hollow nanosphere was successfully prepared, leaving only a small hole in the spherical wall (Figure 1 e). During the formation process of the hollow structure, the release rate of uncrosslinked TA is relatively slow, so that the intact sphere was well preserved. Such hollow spheres with reduction-responsive properties may be used as a nanocarrier for controlled drug release.

In addition, these terpolymers have unique advantages that binary copolymers cannot match. On one hand, the preparation of conventional hollow polyphosphazene microspheres always requires silica spheres, polystyrene spheres, or other nanoparticles as templates.[5] In our current case, hollow nanospheres can be directly prepared without any external template, eliminating the complicated steps and potentially harmful post-treatment processes. On the other hand, the average diameter of the PSTA nanospheres was 50 nm, and the size of other nanospheres obtained using this strategy with changed functional comonomers was also around 50 nm (Figure S8). This was a breakthrough in terms of controlling the size of spherical polyphosphazene materials. The diameters and corresponding comonomers of previously reported cross-linked polyphosphazene microspheres are shown in Table S1 and S2. It can be seen that all of them had the diameter of at least 200 nm. The decreased size would endow the nanomaterials with more fascinating properties. For instance, hollow spheres with small size (such as 50 nm) are more easily phagocytized by cancer cells through enhanced permeability and retention effect to achieve better treatment.[12] The reason why the PSTA nanospheres and their analogues have such smaller particle sizes is mainly due to the existence of the TA component. With a relatively large molecular weight, TA can easily precipitate in the reactions to form primary stable cores in an oligomeric state. According to above-mentioned mechanism, the more primary stable cores achieved in the system, the smaller nanospheres will be obtained.

Different from conventional comonomers bearing two or several nucleophilic groups, TA has abundant catechol groups capable of chelating with metal ions even after crosslinking with HCCP to form the PSTA nanospheres. This post-synthetic metalation offers wider opportunities to tailor the targeted properties of PSTA nanospheres.[13] In the present case, this strategy enables PSTA nanospheres to incorporate various catalytically-active metal centers to achieve PSTA-M nanospheres (M = Co, Ni, or CoNi).

The chemical structures of the obtained products were further characterized using Fourier-transform infrared (FTIR) spectroscopy (Figure S9). It could be inferred that the polycondensation of HCCP, TA and BPS was successfully achieved. The thermal properties of the PSTA and PSTA-Co nanospheres were characterized with thermogravimetric analysis (TGA). As shown in Figure S10, when the specimen

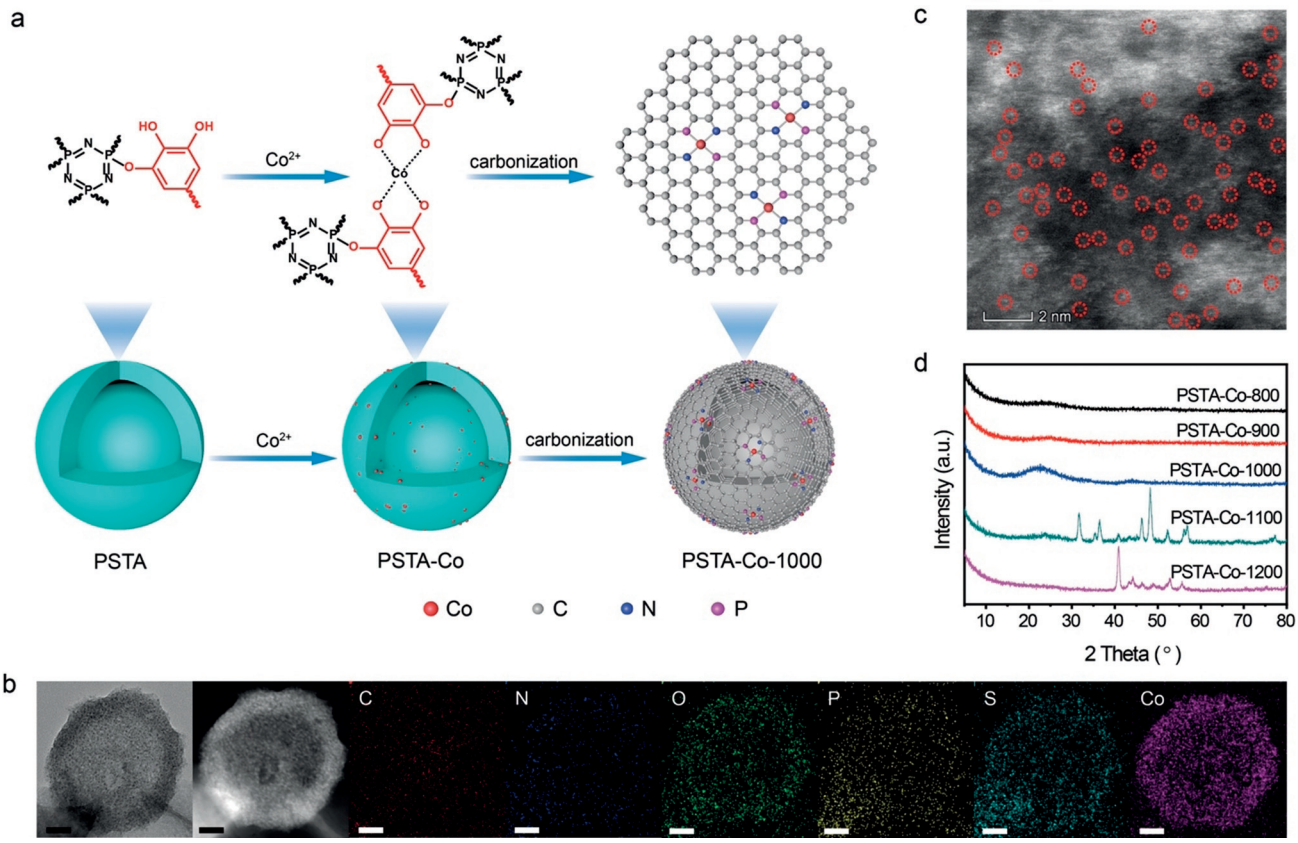

Figure 2. a) Preparation route to PSTA-Co-1000 hollow carbon nanospheres. b) TEM image, HAADF-STEM image and corresponding EDX element mapping of PSTA-Co-1000 nanospheres, scale bar = 10 nm. c) AC HAADF-STEM image of PSTA-Co-1000. Single cobalt atoms are bright dots marked with red circles. d) Powder XRD patterns of PSTA-Co-T (T denotes the carbonization temperature, T = 800, 900, 1000, 1100, or 1200 °C).

was heated up to 800 °C and 1400 °C, the char yield of the PSTA nanosphere was more than 45 % and 35 %, respectively. As for the PSTA-Co nanosphere, the char yield was about 55 % and 38 %, respectively. Both of them had two maximum loss rates at 450 °C and 850 °C. Presumably, aromatic ring structures cross-linked with P/N-heterocyclic rings in the nanospheres endow the PSTA nanosphere with excellent thermal stability, and the metal complexation further strengthens the cross-linked structures for improved thermal stability. The PSTA-M nanospheres were then carbonized to form hollow porous carbon nanospheres as efficient nonprecious metal catalysts for ORR (Figure 2 a). Hollow PSTA, PSTA-Co, PSTA-Ni, and PSTA-CoNi as well as solid SPSTA-Co nanospheres were used as precursors to be directly carbonized at 800 °C under N_2 atmosphere for 3 h. After the acid etching to remove the uncomplexed metals, the carbon nanospheres were further thermally treated at different temperatures (900, 1000, 1100, and 1200 °C) for 3 h to obtain the carbon composite catalysts PSTA-M-T and SPSTA-M-T (T denotes the carbonization temperature: 800, 900, 1000, 1100, or 1200 °C).

The morphology of these carbon composite nanospheres was investigated by field emission scanning electron microscopy (FE-SEM) and TEM as displayed in Figure 2 b and S11–S13. Solid nanospheres maintained a regular spherical morphology after the carbonization. As for the hollow nanospheres, when the treatment temperature was below 1000 °C, carbon nanospheres with spherical hollow cave were obtained. When the temperature increased to 1100 °C, the hollow structure collapsed, forming irregular porous nanospheres (Figure S13). Porous carbon nanospheres with uniform size and hollow structure are desirable for catalytic reactions, because they not only provide more active sites, but also effectively improve the mass transfer efficiency.[14]

HCCP and BPS can introduce heteroatoms such as N, P, and S into the systems, and these heteroatoms coordinate with metals to form active catalytic sites. To date, the heteroatoms in most catalysts are introduced by gridding before the pyrolysis, resulting in uneven distribution of active sites. Since covalently crosslinked heteroatoms are present in the PSTA structure, uniformly dispersed active sites with high population would be obtained after the carbonization.[6a, 14d] Energy dispersive X-ray (EDX) element mapping revealed uniform distribution of Co, P, S, N, O, and C elements in both solid SPSTA-Co-1000 and hollow PSTA-Co-1000 nanospheres (Figure 2 b and S14). The content of Co in PSTA-Co-1000 catalyst was calculated as 10.12 wt % (Table S3).

The porosity of the PSTA-Co nanosphere and its carbonization products was quantified by N_2 adsorption-desorption measurements (Figure S15). The PSTA-Co nanosphere revealed a type V sorption isotherm and the distinct hysteresis

loop indicated a mesoporous feature. In contrast, the PSTA-Co-1000 nanosphere showed a type I sorption isotherm, indicating the micropore-dominated feature. The Brunauer-Emmett-Teller (BET) specific surface area and the pore size of the PSTA-Co-1000 nanosphere were 411.60 $m^2 g^{-1}$ and 0.7 nm, while those of PSTA-Co nanosphere were 51.77 $m^2 g^{-1}$ and 19.75 nm, respectively. Raman spectrum of carbonized PSTA-Co nanospheres presented two peaks at 1362 cm^{-1} and 1587 cm^{-1}, referring to the D and G bands, respectively (Figure S16). The intensity ratio (I_D/I_G) of D and G bands increased from 0.9 to 1.2 when the treatment temperature raised from 800 to 1200 °C, indicating the enrichment of structural defects that might serve as high-performance active sites for electrocatalysis.

Single-atom catalysts, representing the smallest size of metal catalysts, have emerged as a new research frontier in catalysis because of their excellent catalytic performance.[15] In order to confirm the distribution of the metal atoms, the aberration-corrected high-angle annular dark field scanning transmission electron microscopic (AC HAADF-STEM) characterizations were performed (Figure 2c). The results for PSTA-Co-1000 displayed a plenty of well-dispersed speckled bright spots, attributed to transition metals with relatively high atomic numbers, which strongly confirmed the atomic isolation of Co in the obtained PSTA-Co-1000.

Powder X-ray diffraction (XRD) patterns of PSTA-Co-800 to PSTA-Co-1000 showed two broad diffraction peaks at 22° and 44°, corresponding to the C (002) and C (100), indicating complete carbonization of the PSTA-Co nanosphere without the existence of metallic and metal oxide crystals (Figure 2d). In particular, PSTA-Co-1100 and PSTA-Co-1200 showed diffraction peaks corresponding to CoP and Co_2P respectively, meaning the formation of phosphate crystals under high temperature (Figure S17 and S18). X-ray photoelectron spectroscopy (XPS) analysis was performed to evaluate the surface chemical composition and elemental states of different precursors and nanosphere catalysts (Figure S19–S26). The C 1s spectrum exhibited nearly identical curves at different processing steps of samples, indicating good stability of the carbon structure. The N 1s spectrum of PSTA and PSTA-Co showed clear variation from symmetric and sharp peak at 397.9 eV to broader peaks at 398.9 eV and 401.7 eV after Co doping, conforming the metal binding behavior of N atom in the PSTA-Co structure. After the pyrolysis, the N 1 s spectrum revealed the coexistence of graphitic (≈404.9 eV), quaternary (≈401.9 eV), pyrrolic (≈400.9 eV), pyridinic (≈398.4 eV), and metallic (≈399.2 eV) nitrogen species, serving as active sites for ORR. The high-resolution P 2p XPS spectrum of PSTA and PSTA-Co showed the presence of P=N bonding (≈132.1 eV) and P–O bonding (≈132.8 eV), while the spectrum of PSTA-Co-1000 displayed new peaks at 133.6 eV and 131.3 eV, attributed to P–N–C and P–Co coordination, respectively. The O 1s and S 2p spectra revealed the formation and disappearance of their coordination bonds with Co during the steps of Co doping and carbonization, respectively. The peaks around 782.2 and 798.1 eV were assigned to the Co binding with N and P, and no peak could be ascribed to the metallic Co^0 (≈778.3/793.6 eV) nor the oxidized Co (≈780/795 eV) species, verifying that Co exists in the materials through the stable CoN/P coordination.

To confirm the local structure and chemical environment of the catalysts at the atomic level, X-ray absorption fine structure (XAFS) analysis was performed. The Co K-edge X-ray absorption near-edge structure (XANES) curves of PSTA-Co-1000 and references (Co foil, CoO, and Co_3O_4) were shown in Figure 3a. The position of absorption edge for PSTA-Co-1000 indicated that the oxidation state of Co atom was situated nearly between Co^0 and Co^{2+}. As shown in Figure 3b, Fourier transform (FT) k^3-weighted extended X-ray absorption fine structure (EXAFS) for PSTA-Co-1000 showed a relatively broad peak at around 1.79 Å, which could be ascribed to the coexistence of Co-N (1.5 Å) and Co–P (1.88 Å) coordination. Furthermore, the Co–Co peak at about 2.2 Å and other high-shell peaks were not detected, indicating that the Co atom is atomically dispersed in the catalyst. To further confirm the atomic dispersion of Co throughout the whole PSTA-Co-1000, wavelet transform (WT) Co k-edge EXAFS was performed for its ability to distinguish the backscattering atoms even when they overlap substantially in R-space through providing both radial distance resolution and k-space resolution. As shown in Figure 3d–g, WT analysis of PSTA-Co-1000 showed only one intensity maximum at about 6 $Å^{-1}$, which could be ascribed to the Co-N/P coordination. No intensity maximum for the Co–

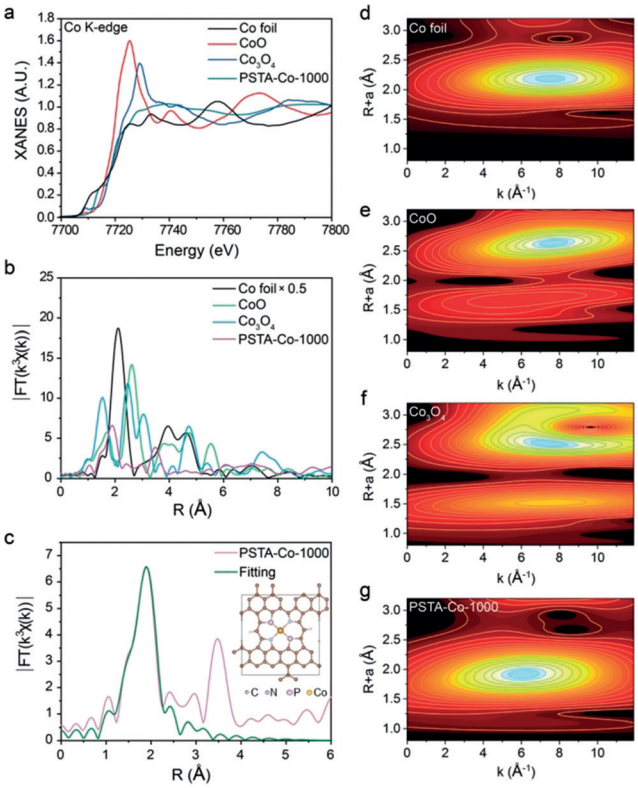

Figure 3. a) Co K-edge XANES and b) FT k3-weighted EXAFS spectra of PSTA-Co-1000, Co foil, CoO, and Co3O4. c) FT-EXAFS fitting curves of PSTA-Co-1000 at R space. Inset is a schematic model of Co-N2P2 site in PSTA-Co-1000. d–g) WT EXAFS of Co foil, CoO, Co3O4, and PSTA-Co-1000, respectively.

Co bonding could be observed, which was distinct from the features of the Co foil, CoO, and Co_3O_4 samples, suggesting complete absence of crystalline metal structures in PSTA-Co-1000. For obtaining quantitative structural parameters of Co atom in PSTA-Co-1000, the EXAFS fitting analysis was conducted. As displayed in Figure 3c and S27–S29 as well as Table S4, the fitting results clearly showed that the main peak at 1.79 Å was originated from Co–N and Co–P first shell coordination with an average coordination number of 2.1 and 1.9, respectively. Accordingly, the structure model of the atomically dispersed Co–N/P site was then illustrated in Figure 3c.

In order to verify the generality of the post-synthetic metalation strategy to obtain PSTA-M and subsequent carbonization to afford single atomic metal sites stabilized on N/P co-doped carbon materials, other metal precursors were chosen to replace $Co(OAc)_2$. As shown in Figure S30 and S31, the PSTA-Ni and bimetal doped PSTA-Co/Ni nanospheres were successfully prepared. Correspondingly, the HAADF-STEM images (Figure S32 and S33) demonstrated the successful formation of well-distributed single metal atoms in the obtained materials by the carbonization.

Electrocatalytic ORR properties of the PSTA-Co nanosphere derived catalysts were evaluated using a rotating disk electrode technique in 0.1M KOH. Cyclic voltammetry (CV) curves revealed a distinct oxygen reduction peak in the O_2 saturated solution, implying high oxygen reduction activity of PSTA-Co-1000 (Figure S34). Linear sweep voltammogram (LSV) curve for PSTA-Co-1000 at the rotating speed of 1600 rpm showed its half-wave potential and limiting current density at 0.878 V and 6.4 mA cm^{-2}, respectively (Figure 4a). Such values were superior to that of commercial Pt/C (0.832 V, 5.4 mA cm^{-2}) and made PSTA-Co-1000 one of the best nonprecious metal ORR catalysts reported so far (Table S5). The solid sample (SPSTA-Co-1000), metal free sample (PSTA-1000), and PSTA-Co spheres carbonized under various temperatures were also tested for comparison. Their lower ORR activities demonstrated the significance of the mesoporous hollow structure and well-dispersed single cobalt sites from PSTA-Co-1000. LSV curves of PSTA-Co-1000 were then obtained at different rotation rates to investigate the kinetics of the ORR activity (Figure 4b). The limiting current density increased upon increasing the rotation rate from 1000 to 2000 rpm. Corresponding Koutecky–Levich (K–L) plots (Figure 4c) exhibited good linearity, and the electron transfer number was about 3.9, suggesting a four-electron transfer pathway for ORR. PSTA-Co-1000 exhibited superior catalytic durability than Pt/C. As shown in Figure S35, after 10000 continuous cycles, the half-wave potential of PSTA-Co-1000 only showed slight shifting ($\approx$5 mV), much less than that of Pt/C ($\approx$25 mV). Powder XRD patterns and HAADF-STEM images exhibited that the single Co active sites were still homogeneously dispersed after the accelerated durability test (Figure S36 and S37). In addition, PSTA-Co-1000 revealed high resistance to the methanol crossover effect. While an obvious change occurred for the Pt/C catalyst after injecting methanol into the electrolyzing solution, a negligible response was observed in the case of PSTA-Co-1000 (Figure 4d). Furthermore, the PSTA-Co-1000 also displayed a good ORR activity in acidic solution (0.1M $HClO_4$, Figure S38 and S39).

To theoretically understand the ORR activity nature of PSTA-Co-1000, first principle density functional theory (DFT) calculations were conducted. The control model of Co-N_4 was built for comparison with Co-N_2P_2. As illustrated in Figure 5a and Table S6, the free energy diagram of ORR on Co-N_2P_2 and Co-N_4 exhibited a consistent downhill energy profile at $U=0$ V, indicating a stable exothermal process. The highest ΔG from the second electron transfer sub-step (HOO*–O) demonstrated the rate determining step at $U=$ 1.23 V. Co-N_2P_2 possessed lower ΔG (0.271 eV) than that of

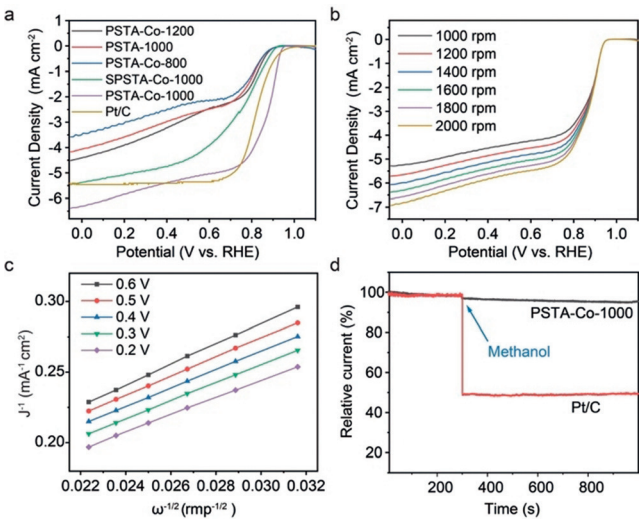

Figure 4. a) LSV curves of PSTA-Co-T ($T=$800, 1000, and 1200°C), PSTA-1000, SPSTA-Co-1000, and Pt/C at a rotating speed of 1600 rpm. b) LSV curves of PSTA-Co-1000 at different rotating speeds. c) K-L plots of PSTA-Co-1000. d) Tolerance to methanol by PSTA-Co-1000 as compared with the Pt/C electrocatalyst, where the arrow indicates the injection time of methanol.

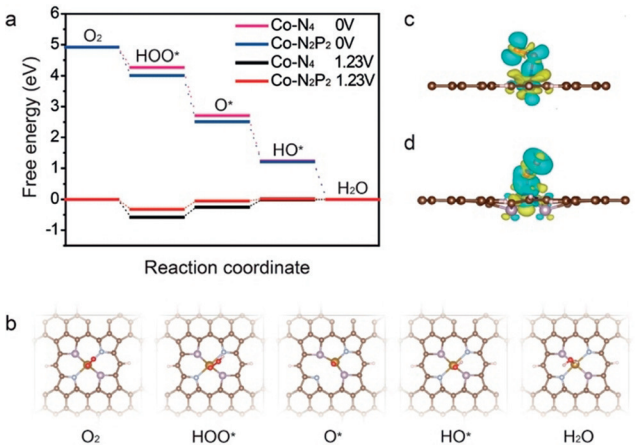

Figure 5. a) ORR free energy profiles of a Co-N_2P_2 site in PSTA-Co-1000 as compared with a Co-N_4 site at zero potential and equilibrium potential ($U=$1.23 V). b) Illustrative ORR pathway on PSTA-Co-1000. The differential charge density of O_2 adsorbed on c) a Co-N_4 site and d) a Co-N_2P_2 site. Electron accumulation is in blue, and electron depletion in yellow.

Co-N_4 (0.33 eV), suggesting more efficient ORR catalytic activity of Co-N_2P_2.[16] As shown in Figure 5b and S40 as well as Table S7, O_2 molecule was adsorbed on the Co-N_2P_2 site in the end-on model with a moderate adsorption free energy (ΔG O_2) of −0.27 eV, which was lower than that on the Co-N_4 site (−0.13 eV). On the contrary, the adsorption energy of H_2O on the Co-N_2P_2 and Co-N_4 sites was 1.36 eV and 0.62 eV, respectively. The results indicated that Co-N_2P_2 could bind O_2 more efficiently to initiate the ORR and bind H_2O weakly to complete the reaction. The differential charge density maps (Figure 5c,d and S41) showed that more electrons would accumulate on O_2 when it adsorbed on the Co-N_2P_2 structure, which was beneficial to the reduction of O_2.[17] The ORR overpotential on the catalytic sites was further calculated with the DFT model. A significantly lower overpotential value was obtained on Co-N_2P_2 (0.58 V) as compared with that on Co-N_4 (0.32 eV), indicating much faster ORR kinetics on N/P co-doped PSTA-Co-1000 catalyst.

Conclusion

In summary, we have demonstrated a facile template-free method to construct cross-linked polyphosphazene spheres with both nanosized diameter and uniform hollow structure. This method allows for the synthesis of various cross-linked polyphosphazene nanospheres with tunable properties by using different functional co-monomers bearing dual/multi-nucleophilic groups to polymerize with HCCP and TA. After forming PSTA nanospheres, the unreacted catechol groups on TA could chelate with metal ions to introduce a range of catalytically-active metal centers. Upon further carbonization, the obtained carbon nanospheres with mesoporous hollow structure, small particle size ($\approx$50 nm), high surface area (411.60 $m^2 g^{-1}$), and well-dispersed single atom Co-N_2P_2 sites have exhibited remarkable electrocatalytic ORR activities including high current density, excellent durability, and superior methanol tolerance. This work not only provides a straighthood route for the synthesis of diverse polyphosphazene nanospheres, but also offers a feasible pathway to achieve N/P co-coordinated single metal atom doped hollow carbon nanospheres for electrochemical applications.

Acknowledgements

This research was supported by the National Natural Science Foundation of China (51773170 and 21701130), and the Singapore National Research Foundation Investigatorship (NRF-NRFI2018-03). We also thank the Analytical & Testing Center of Northwestern Polytechnical University for equipment support and Shiyanjia Lab (http://www.shiyanjia.com) for the XAFS tests and DFT calculations.

Conflict of interest

The authors declare no conflict of interest.

Keywords: electrocatalysis · hollow porous nanospheres · oxygen reduction reaction · polyphosphazene · single atom catalysts

[1] a) L. Zhu, Y. Xu, W. Yuan, J. Xi, X. Huang, X. Tang, S. Zheng, *Adv. Mater.* **2006**, *18*, 2997–3000; b) P. Mohanty, L. D. Kull, K. Landskron, *Nat. Commun.* **2011**, *2*, 401.
[2] C. Wan, X. Huang, *Mater. Today Commun.* **2017**, *11*, 38–60.
[3] a) W. Wei, X. Huang, X. Zhao, P. Zhang, X. Tang, *Chem. Commun.* **2010**, *46*, 487–489; b) L. Sun, T. Liu, H. Li, L. Yang, L. Meng, Q. Lu, J. Long, *ACS Appl. Mater. Interfaces* **2015**, *7*, 4990–4997; c) S. Qiu, Y. Zhou, X. Zhou, T. Zhang, C. Wang, R. K. K. Yuen, W. Hu, Y. Hu, *Small* **2019**, *15*, 1805175.
[4] a) J. Fu, X. Huang, Y. Huang, J. Zhang, X. Tang, *Chem. Commun.* **2009**, 1049–1051; b) X. Huang, W. Wei, X. Zhao, X. Tang, *Chem. Commun.* **2010**, *46*, 8848–8850; c) X. Wei, H. Chen, H. P. Tham, N. Zhang, P. Xing, G. Zhang, Y. Zhao, *ACS Appl. Nano Mater.* **2018**, *1*, 3663–3672; d) X. Wei, G. Zhang, L. Zhou, J. Li, *Appl. Surf. Sci.* **2017**, *419*, 744–752.
[5] J. Fu, Q. Xu, J. Chen, Z. Chen, X. Huang, X. Tang, *Chem. Commun.* **2010**, *46*, 6563–6565.
[6] a) J. Wei, G. Wang, F. Chen, M. Bai, Y. Liang, H. Wang, D. Zhao, Y. Zhao, *Angew. Chem. Int. Ed.* **2018**, *57*, 9838–9843; *Angew. Chem.* **2018**, *130*, 9986–9991; b) H. Yang, S. J. Bradley, X. Wu, A. Chan, G. I. N. Waterhouse, T. Nann, J. Zhang, P. E. Kruger, S. Ma, S. G. Telfer, *ACS Nano* **2018**, *12*, 4594–4604; c) J. Wei, Y. Liang, Y. Hu, B. Kong, G. P. Simon, J. Zhang, S. P. Jiang, H. Wang, *Angew. Chem. Int. Ed.* **2016**, *55*, 1355–1359; *Angew. Chem.* **2016**, *128*, 1377–1381.
[7] a) G. Wang, J. Qin, X. Zhou, Y. Deng, H. Wang, Y. Zhao, J. Wei, *Adv. Funct. Mater.* **2018**, *28*, 1806144; b) T. Liu, W. Liu, M. Zhang, W. Yu, F. Gao, C. Li, S. B. Wang, J. Feng, X. Z. Zhang, *ACS Nano* **2018**, *12*, 12181–12192; c) J. Kim, K. R. Kim, Y. Hong, S. Choi, C. T. Yavuz, J. W. Kim, Y. S. Nam, *ACS Appl. Mater. Interfaces* **2019**, *11*, 21915–21925.
[8] M. Shin, H. A. Lee, M. Lee, Y. Shin, J. J. Song, S. W. Kang, D. H. Nam, E. J. Jeon, M. Cho, M. Do, S. Park, M. S. Lee, J. H. Jang, S. W. Cho, K. S. Kim, H. Lee, *Nat. Biomed. Eng.* **2018**, *2*, 304–317.
[9] a) H. Yang, S. J. Bradley, A. Chan, G. I. Waterhouse, T. Nann, P. E. Kruger, S. G. Telfer, *J. Am. Chem. Soc.* **2016**, *138*, 11872–11881; b) Y. Shi, Y. Yu, Y. Liang, Y. Du, B. Zhang, *Angew. Chem. Int. Ed.* **2019**, *58*, 3769–3773; *Angew. Chem.* **2019**, *131*, 3809–3813; c) C. Zhu, E. Chalmers, L. Chen, Y. Wang, B. B. Xu, Y. Li, X. Liu, *Small* **2019**, *15*, 1902440.
[10] a) F. Guo, H. Yang, L. Liu, Y. Han, A. M. Al-Enizi, A. Nafady, P. E. Kruger, S. G. Telfer, S. Ma, *J. Mater. Chem. A* **2019**, *7*, 3624–3631; b) X. Jia, J. Wu, K. Lu, Y. Li, X. Qiao, J. Kaelin, S. Lu, Y. Cheng, X. Wu, W. Qin, *J. Mater. Chem. A* **2019**, *7*, 14302–14308; c) Y. J. Tang, H. J. Zhu, L. Z. Dong, A. M. Zhang, S. L. Li, J. Liu, Y. Q. Lan, *Appl. Catal. B* **2019**, *245*, 528–535.
[11] a) G. Wu, K. L. More, C. M. Johnston, P. Zelenay, *Science* **2011**, *332*, 443–447; b) J. R. Selman, *Science* **2009**, *326*, 52–53; c) Z. Yang, Y. Wang, M. Zhu, Z. Li, W. Chen, W. Wei, T. Yuan, Y. Qu, Q. Xu, C. Zhao, X. Wang, P. Li, Y. Li, Y. Wu, Y. Li, *ACS Catal.* **2019**, *9*, 2158–2163; d) J. Wang, W. Liu, G. Luo, Z. Li, C. Zhao, H. Zhang, M. Zhu, Q. Xu, X. Wang, C. Zhao, Y. Qu, Z. Yang, T. Yao, Y. Li, Y. Lin, Y. Wu, Y. Li, *Energy Environ. Sci.* **2018**, *11*, 3375–3379.
[12] L. Pan, J. Liu, J. Shi, *Chem. Soc. Rev.* **2018**, *47*, 6930–6946.
[13] J. D. Evans, C. J. Sumby, C. J. Doonan, *Chem. Soc. Rev.* **2014**, *43*, 5933–5951.
[14] a) T. T. Sun, S. Zhao, W. X. Chen, D. Zhai, J. C. Dong, Y. Wang, S. L. Zhang, A. J. Han, L. Gu, R. Yu, X. D. Wen, H. L. Ren, L. B. Xu, C. Chen, Q. Peng, D. S. Wang, Y. D. Li, *Proc. Natl. Acad. Sci. USA* **2018**, *115*, 12692–12697; b) Y. Chen, Z. Li, Y. Zhu, D. Sun,

X. Liu, L. Xu, Y. Tang, *Adv. Mater.* **2019**, *31*, 1806312; c) B. W. Zhang, T. Sheng, Y. D. Liu, Y. X. Wang, L. Zhang, W. H. Lai, L. Wang, J. Yang, Q. F. Gu, S. L. Chou, H. K. Liu, S. X. Dou, *Nat. Commun.* **2018**, *9*, 4082; d) L. Zhang, J. Fischer, Y. Jia, X. Yan, W. Xu, X. Wang, J. Chen, D. Yang, H. Liu, L. Zhuang, M. Hankel, D. J. Searles, K. Huang, S. Feng, C. L. Brown, X. Yao, *J. Am. Chem. Soc.* **2018**, *140*, 10757 – 10763.

[15] a) A. Zitolo, V. Goellner, V. Armel, M. T. Sougrati, T. Mineva, L. Stievano, E. Fonda, F. Jaouen, *Nat. Mater.* **2015**, *14*, 937 – 942; b) L. Zhao, Y. Zhang, L. B. Huang, X. Z. Liu, Q. H. Zhang, C. He, Z. Y. Wu, L. J. Zhang, J. Wu, W. Yang, L. Gu, J. S. Hu, L. J. Wan, *Nat. Commun.* **2019**, *10*, 1278.

[16] R. Jiang, L. Li, T. Sheng, G. Hu, Y. Chen, L. Wang, *J. Am. Chem. Soc.* **2018**, *140*, 11594 – 11598.

[17] Z. Lu, B. Wang, Y. Hu, W. Liu, Y. Zhao, R. Yang, Z. Li, J. Luo, B. Chi, Z. Jiang, M. Li, S. Mu, S. Liao, J. Zhang, X. Sun, *Angew. Chem. Int. Ed.* **2019**, *58*, 2622 – 2626; *Angew. Chem.* **2019**, *131*, 2648 – 2652.

Manuscript received: April 29, 2020
Accepted manuscript online: June 2, 2020
Version of record online: July 1, 2020

